Journal of Solid State Chemistry 318 (2023) 123741

Contents lists available at ScienceDirect

Journal of Solid State Chemistry

journal homepage: www.elsevier.com/locate/jssc

Investigation of physical and electrochemical properties of Ni-doped Tunnel/P2 hybrid $Na_{0.44}MnO_2$ cathode material for sodium-ion batteries

Erdinc Oz [a,b,*], Serdar Altin [c], Sevda Avci [d]

[a] Ataturk University, Physics Department, 25400, Erzurum, Turkey
[b] Ataturk University, Nanoscience and Nanoengineering Department, 25400, Erzurum, Turkey
[c] Inonu University, Physics Department, 44210, Malatya, Turkey
[d] Istanbul Medeniyet University, Department of Engineering Physics, 34720, Istanbul, Turkey

ARTICLE INFO

Keywords:
Sodium-ion batteries
Hybrid materials
Ni substitution
Cycle life

ABSTRACT

The increasing demand for energy in recent years has accelerated the efforts to increase the efficiency of energy storage systems. Although lithium-ion batteries are very popular in energy storage systems, the dramatic increase in costs due to the decrease in lithium resources has greatly increased the interest in sodium-ion batteries. $Na_{0.44}MnO_2$ has recently received increasing attention due to the fact that the tunnel structures in the crystal structure are suitable for the diffusion of Na ions. However, rapid structural degradation is an important problem that must be overcome to move into practical applications. In this study, the tunnel/P2 hybrid type $Na_{0.44}MnO_2$ was synthesized by a one-step heat treatment with the Ni substitution to Mn sites for improving cyclic performance. It was demonstrated by various physical analyses, that biphasic hybrid material starts forming with Ni substitution, and Ni occupied the Mn sites in the P2 phase. Electrochemical measurements provide that after 100 cycles at 0.3C, while $Na_{0.44}MnO_2$ has 77% capacity retention, 1% and 5% Ni substituted samples have 86.4% and 77.3%, respectively. The results show that tunnel-P2 hybrid cathode materials can be developed for practical applications in sodium-ion batteries.

1. Introduction

Fossil fuels are an important factor in global climate change in the last years, due to the, increasing energy demands causing renewable energy technologies to develop rapidly. Although there have been advanced developments in the variety of renewable energy sources, such as solar and wind energy, it is important to consider the storage and transport of the energy produced from these sources. In recent decades, lithium-ion batteries (LIBs) have been used on a large scale for the storage and transportation of energy, such as in portable electronic devices and electric vehicles. However, the continuous increase in the cost of lithium and the reduction of resources hinders the work on large-scale energy storage and transmission systems. Sodium ion batteries (SIBs) are the most interesting energy storage systems in the search for alternatives to LIBs. A reason for this attractiveness is that sodium is one of the most abundant elements in the world's crust and therefore costs less than lithium. Another reason is that the system used in SIBs has the same working principle as that of LIBs and is therefore easy to develop. Furthermore, large-scale energy storage systems do not need the high volumetric density as the portable devices do. Hence, the usage of SIBs instead of LIBs in large-scale systems is more advantages than LIBs.

Many positive electrode materials, such as layered transition metal oxides, organic polymers and Prussian blue, were evaluated for their potential use in sodium batteries. Among them, the tunnel-type transition metal oxide $Na_{0.44}MnO_2$ (NMO) was highly promising because it not only has an ideal crystalline structure for sodium addition/removal reactions [1,2]but has a high theoretical capacity (121 mAh/g) [3]. This unique cathode material has been synthesized by different methods, such as hydrothermal [4], electrospun [5], sol-gel [6], spray pyrolysis [7], and modified-Pechini method [8,9]. Apart from these methods, it was synthesized by the solid-state reaction method, and tested as an aqueous electrode, and has been observed that it has 99.7 mAh/g capacity after 800 cycles at 1C [10].

The advantages of the NMO compound are that the reduction/oxidation reaction area increases due to the large surface area and the short diffusion distance because of its rod-like structure. However, deformations in the crystal structure cause capacity fades because of the large ionic radius of the Na ion and the Jahn-Teller (JT) effect on the

* Corresponding author. Ataturk University, Physics Department, 25400, Erzurum, Turkey
E-mail address: erdinc.oz@atauni.edu.tr (E. Oz).

https://doi.org/10.1016/j.jssc.2022.123741
Received 17 October 2022; Received in revised form 18 November 2022; Accepted 21 November 2022
Available online 24 November 2022
0022-4596/© 2022 Elsevier Inc. All rights reserved.

octahedral Mn^{+3} [11]. The JT effect causes structural deformation and increased capacity loss in long cycle numbers by acting on Mn^{+3} ions in the octahedral structure, especially during the charge/discharge cycle [12,13]. One of the solutions developed to solve this problem is to make cation substitution. It has been tried to overcome the structural degradation issue by substituting Mn^{+3} ions with ions that have no JT effect. Yu, Gu and Hu et *al.* made Ti substitutions in the Mn^{+3} sites of the NMO sample and examined the charge/discharge profile. The results reveled that Ti doping disrupts the charge order and reduces the storage voltage, and this material can be used as an anode in sodium batteries [14].

The layered P2–$Na_{0.7}MnO_{2.05}$ is an attractive material because of its 200 mAh/g specific capacity and high volumetric capacity [15]. However, phase transitions from P2 to O2 at high voltage cause capacity loss during charge/discharge. Moreover, the distortion of the orthorhombic structure because of JT effect on Mn^{+3} induces capacity loss [16]. To reduce the JT effect and increase the structural stability, substitution of different cations for Mn^{+3} has been reported. Nazar et *al.* made Li substitution for Mn in P2–$Na_{0.6}MnO_2$ to suppress the JT effect and obtained 196 mAh/g at the end of 100 cycles in the range of 2–4.6 V [17]. They reported that Li substitution suppresses structural degradation during charge/discharge cycle. Similarly, Passerini et *al.* successfully synthesized 11% Mg substituted P2-$Na_xMg_{0.11}Mn_{0.89}O_2$ and reported 99.5% Coulombic efficiency at the end of 200 cycles [18].

Ni is one of the ideal transition metals that can be substituted for Mn, as it is not exposed to the JT effect of Ni^{+3} spin configurations in the octahedral environment. The presence of MnO_6 octahedral structures in both P2–$Na_{0.7}MnO_{2.05}$ and NMO crystal structures make Ni substitution ideal for suppressing the JT effect for both crystal structures. Guo et al. reported that Ni substituted to Mn sites in the octahedral structure in the $K_{0.67}MnO_2$ material increased the structural stabilization by suppressing the JT effect, and as a result, 75% capacity retention performance was observed in the 200 cycle high rate test [19].

The hybrid cathode materials are seen in recent studies as a new approach in terms of capacity enhancement and stable crystal structure for rechargeable batteries. Lee et al. [20] investigated the structural and electrochemical properties of the layered-spinel structure $Mn_{1.5}Ni_{0.425}Co_{0.075}$ composite cathode material for LIBs and reported that the layered structure turns into spinel structure and the original spinel structure does not show Jahn-Teller distortion during charging, therefore, the composite material shows superior structural stability in the high voltage range of 2–5 V. Furthermore, Wu et al. investigated Mn based hybrid layered-tunnel structure for Na-ion batteries and demonstrated that this hybrid structure provides 83.3 mAh/g after 700 cycles at 10C [21]. On the other hand, Guo et *al.* doped Zr to both compounds in hybrid cathode material and investigated the rate performance [22]. The $Na_{0.6}Mn_{1-x}Zr_xO_2$ (x = 0, 0.02 and 0.05) series was synthesized using the co-precipitation method and the P2-tunnel hybrid structure was obtained, The results show that the Zr^{+4} ions were substituted into both the P2 structure and the tunnel structure successfully. The Zr^{+4} substitution for Mn^{+4} increases the energy of metal-oxygen bonds and enhances the rate capability, especially in full cell [22].

In this study, we showed that $Na_{0.44}Mn_{0.99}Ni_{0.01}O_2$ (NMNO1) and $Na_{0.44}Mn_{0.95}Ni_{0.05}O_2$ (NMNO5) tunnel-P2 type hybrid materials can be used as positive electrode in sodium-ion batteries. We proved Ni substitutions at Mn sites in the P2 structure using special analyzing methods and investigated battery performances with electrochemical techniques.

2. Experimental

2.1. Material synthesis

All materials were synthesized by the two-step solid-state reaction method using Na_2CO_3 (Sigma, > 99%), $MnCO_3$ (Sigma, > 99%), NiO (Sigma, > 99%) precursors, weighed with a precision balance (10 wt% excess Na_2CO_3 was used to compensate for the Na loss during high-temperature synthesis). In the first step, the powder precursors mixed with the ball mill were placed in the alumina boat and calcination heat treatment was carried out at 300 °C for 1 h. Then, in order to achieve homogenization for the second step, the powder mixture was mixed with a ball mill for one more hour and the mixture was heated up to 800 °C for 9 h. After heat treatment, the samples were transferred to the glove-box due to moisture sensitivity.

2.2. Physical characterization

X-ray Diffraction (XRD) data were collected at the DESY synchrotron facility at beamline P02.1 (Hamburg, Germany) using the XRD 1624 detector (PerkinElmer) at fixed wavelength (λ) 0.2066 Å and calibration made by standard material LaB_6. For measurements, the samples were brought into fine powder form and placed in Kapton tubes. During the measurement, the tubes were rotated and 60 s exposure time was used to increase the number of data. Crystal structure analyzes of the samples were made with the Rietveld refinement method using FullProf software [23].

The morphologies of the samples were examined by scanning electron microscopy (EVO 40 XVP, LEO, 30 kV). Detailed structure analysis was determined by both a transmission electron microscope (TEM) and a high-resolution scanning electron microscope (HRTEM) with selected area electron diffraction (SAED) module (JEM-2011, 200 kV) at Universitat Autonoma de Barcelona. Raman spectra were recorded with the Senterra microscope (RIGAKU) using a 532 nm laser in working electrode form. Temperature dependent magnetization (M-T) measurements were performed with the vibrating sample magnetometer (VSM) option of the physical property measurement system (PPMS) device (Quantum Design) under 1 kOe magnetic field at various temperature (5–300 K).

The spectra of Mn K-edge were collected by X-ray Absorption Spectroscopy (XAS) technique at P64 beamline of the DESY PETRA III (Hamburg, Germany) in fluorescence mode at room temperature. The radiation was monochromatized using a liquid nitrogen cooled double-crystal monochromator (DCM) (Si (111) single-crystal). To obtain acceptable quality spectra, each XAS measurement was repeated three times and averaged.

X-ray photoelectron (XPS) measurements were performed using a monochromatized Al-Kalpha x-ray source (1486.6 eV) with Thermo Fisher K-Alpha spectrometer (SuzerLab, Bilkent University). A detailed measurement description and fitting procedure can be found in the literature [24]. Sample powders were stuck on the sample holder of the XPS spectrometer. Pass energy was set at 200 eV for the survey spectrum and 50 eV for core-level measurements.

2.3. Electrochemical characterization

Cathode slurries were made by mixing the active materials (80 wt%: 10 wt %: 10 wt %), carbon black and the polyvinylidene fluoride (PVDF) binder with the N-methy1-2-pyrrolidone (NMP) as a solvent. The slurry was applied on the Al foil and was dried at 120 °C under vacuum overnight to remove the NMP completely. Discs with a diameter of 10 mm were punched and used as working electrodes. Each working electrode contains 3.0–3.5 mg active material.

CR2032 type coin cell form was used for electrochemical tests. In 10 mm diameter disk shape punched sodium metal as an anode, Whatman GF/D as a separator, 1 M $NaClO_4$ salt dissolved in ethylene carbonate (EC)/propylene carbonate (PC) (1: 1 w/w) used as electrolyte. The cells were assembled in an argon-filled glove box.

Cyclic voltammetry (CV) measurements were carried out using a VMP3 multichannel potentiostat (BioLogic) with 0.1 mV/s scan rate at a 2.0–4.0 V potential window. Galvanostatic charge-discharge tests were performed using Octastat multichannel potentiostat (Iviumstat) in the potential range 2.0–4.0 V at C/3 rate (1C = 121 mAh/g) at room temperature at AltinLab Inonu University.

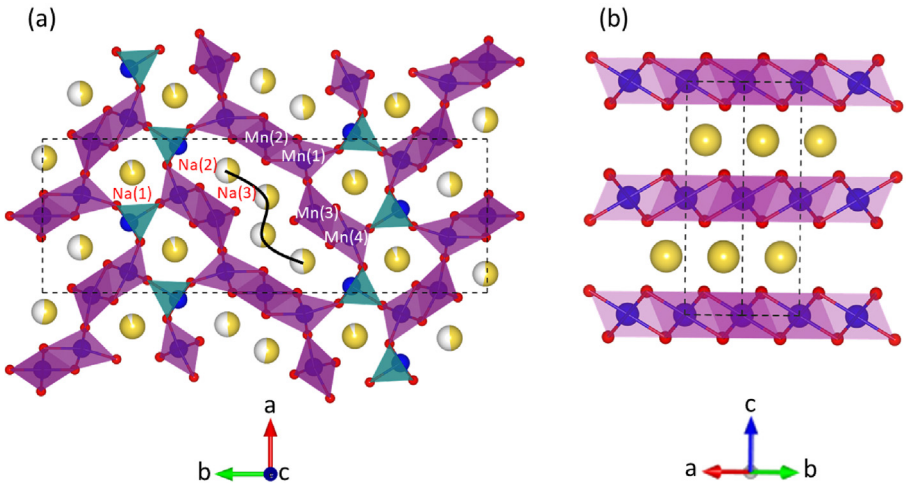

Fig. 1. (a) Tunnel type $Na_{0.44}MnO_2$ and (b) layered P2-type $Na_{0.7}MnO_2$ crystal structure. The yellow, blue and red spheres indicate Na, Mn and O atoms, respectively. The Mn atoms are located only in octahedral structure in P2 type structure, they are in both octahedral (purple) and square pyramid structures (green) in tunnel type structure.

3. Results and discussion

Fig. 1 shows tunnel type $Na_{0.44}MnO_2$ and P2 type $Na_{0.7}MnO_{2.05}$ crystal structure. Mn atoms are located on sites with MnO_6 octahedral and MnO_5 square pyramid symmetries in NMO structure (Fig. 1(a)). Region (1), (5) and (2) are occupied by Mn^{+4}, while (3) and (4) are occupied by Mn^{+3}, thereby ensuring charge neutrality [25]. While sodium intercalation/deintercalation, MnO_6 octahedral structures play an active role, while MnO_5 structure provides stability of the crystal structure [26]. On the sodium side, there are three different sites: Na1 is in a small tunnel-like structure, while Na2 and Na3 are located in a S-shaped tunnel structure [27]. While Na2 and Na3 play a role in insertion/extraction, this is quite difficult for Na1 [28].

$Na_{0.7}MnO_{2.05}$ has a layered structure consisting of corner-shared and edge-shared MnO_6 octahedra (Fig. 1(b)) [29]. Each oxygen atom in Mn-centered octahedral structures is shared with three different Mn atoms, and Na ions fill the spaces between the octahedral layers [30].

Refinement results showed that lattice parameters decreased with the increase of Ni substitution of the $Na_{0.44}MnO_2$ phase. The reason for this may be that the amount of Na is calculated based on the $Na_{0.44}MnO_2$ phase during the synthesis and these Na ions are used in the formation of the P2 phase. For this reason, $Na_{0.44}MnO_2$ phase may have decreased in Na and degraded the structure and decreased in volume. The reason for the decrease in the lattice parameter of the P2 phase is the fact that the ionic radius of Ni^{+3} is smaller than Mn^{+3}, which will be explained in detail later.

Rietveld refinement result of the NMO, NMNO1 and NMNO5 samples are shown in Fig. 2. The results confirm that the NMO sample has phase purity within an orthorhombic structure (*Pbam* space group). The lattice parameters are calculated as a = 9.1321(1) Å, b = 26.4474(4) Å and c =

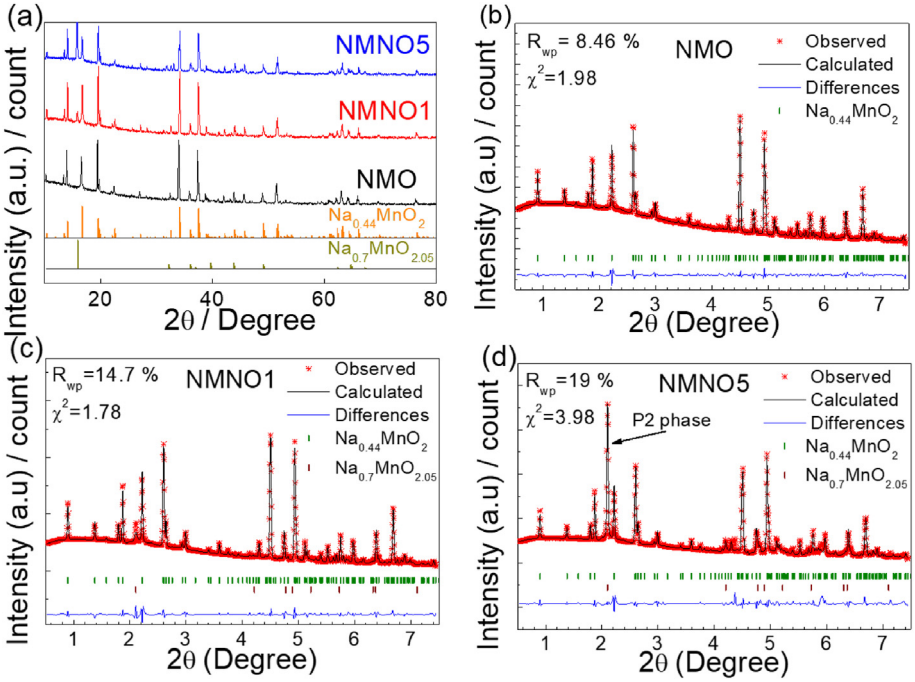

Fig. 2(a). XRD pattern of NMO, NMNO1 and NMNO5 samples. The patterns belong to the standard phases of $Na_{0.44}MnO_2$ (ICSD-261314) and $Na_{0.7}MnO_{2.05}$ (PDF-27-0751) seen at the bottom. Results from Rietveld refinement can be seen for (b) NMO, (c) NMNO1 and (d) NMNO5. Refinement parameters are quite acceptable values.

Table 1
Phase ratio and lattice parameters of samples.

Sample	Phases (%ratio)	$Na_{0.44}MnO_2$	
		Lattice Parameters (Å)	Volume (Å^3)
NMO	$Na_{0.44}MnO_2$(%100)	a = 9.1321 (54) b = 26.4474 (16) c = 2.8339 (11	684.47 (64)
NMNO1	$Na_{0.44}MnO_2$(%73.57) $Na_{0.7}MnO_{2.05}$(%26.43)	a = 9.1234 (43) b = 26.4356(13) c = 2.8332 (98)	683.326 (52)
NMNO5	$Na_{0.44}MnO_2$(%73.54) $Na_{0.7}MnO_{2.05}$(%26.46)	a = 9.1136 (25) b = 26.4606 (75) c = 2.8309 (88)	682.687 (96)

2.83390(4) Å and they are in well agreement with the previous studies [31,32]. In the synchrotron XRD data, reflection that belongs to the P2 phase emerges at 2.1° in NMO1 sample and its intensity increases with increasing Ni content as presented in Fig. 2(c) and d. Wu and Chen [33] reported similar P2 phase transition in $Na_{0.44}MnO_2$ for 1% Mg doping. Impurity phases were not detected in samples. The lattice parameters obtained, according to the refinement results and the phase percentages are listed in Table 1, and $Na_{0.7}MnO_{2.05}$ phase percentage and lattice parameters in NMNO1 and NMNO5 are listed in Table S1.

Fig. 3(a) shows detailed morphology images of NMNO1 sample. The sample contains both P2 and nanorod structure, as seen in the XRD results. While NMO sample does not contain P2 structure, NMNO5 has P2 and nanorod structures similar to NMNO1. The mapping and TEM images of both samples are shown in Figs. S1 and S2. Although the samples in Fig. 3 (a)–(d), NMO and NMNO1 are nanorod-like, the average widths of these nanorod-like structures were measured as 485(97) nm, 613(88) nm and 1022 (20) nm for NMO, NMNO1 and NMNO5, respectively. As seen in the HRTEM image in Fig. 3(a), the interplanar distance is 0.440-nm-long corresponding to the (200) plane [6,34] that is parallel to the growth direction [001]. SAED images from regions (1) and (2) in the Figure show that P2 and T structure crystallize well. According to the EDS results from the same regions (Fig. 3(b)), Ni atoms are substituted in the P2 structure instead of nanorods. This result is also clearly seen from the high Ni count in the P2 structure in the mapping results taken from the NMN1 sample (Fig. 3 (c)).

Ni substitution for Mn in the octahedral structure of MnO_6 in the P2 phase affects Mn^{+3}/Mn^{+4} ratio and therefore it is important to understand the change of JT effect on the crystal structure [26]. In theory, the $Na_{0.7}MnO_{2.05}$ phase contains Mn^{+3} and Mn^{+4} ions to ensure charge neutrality. If Ni atoms are substituted, this should theoretically be between Mn^{+3} and Ni^{+3}. This is because the Ni^{+3} ion has an ionic radius of 0.56 nm, while the Mn^{+3} and Mn^{+4} ions have ionic radii of 0.58 and 0.53 nm [35], respectively, and therefore, Ni^{+3} tends to be substituted by Mn^{+3} ions. On the other hand, the results of the magnetism measurements show that the effective magnetic moment (μ_{eff}) of the samples increases with increasing Ni content (Fig. S2). It has been discussed in detail in the SI that this situation can only be realized by substitution of Ni^{+3} to Mn^{+3} sites. Moreover, analysis of the substitution of Ni^{+3} for Mn^{+3} sites will be discussed in the next sections.

Raman spectroscopy results provide information about the formation of the samples (Fig. 3(d)). The Raman shifts and associated vibration

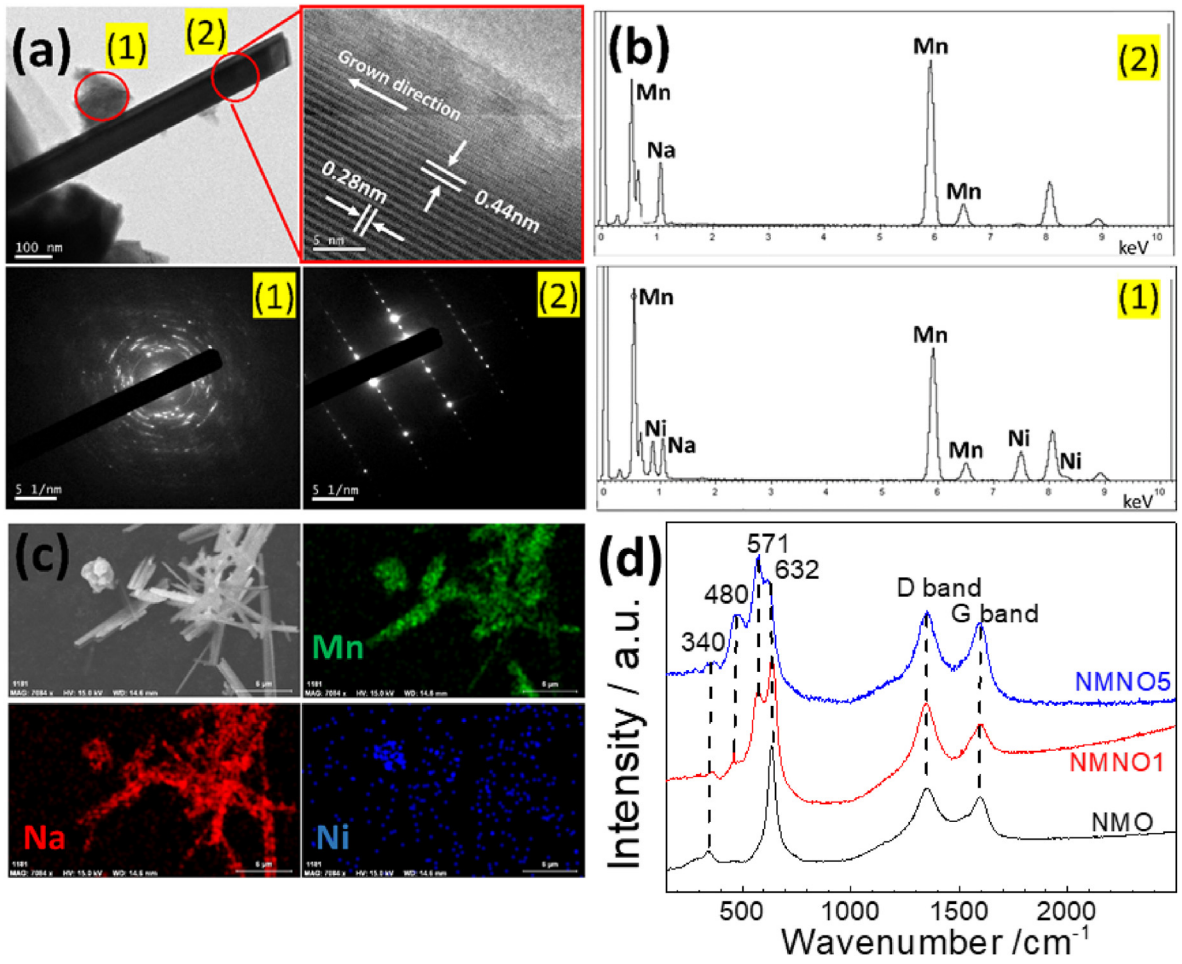

Fig. 3. (a) TEM, HRTEM and SAED images, (b) EDS result of specified area in TEM image of NMNO1 sample. Mapping results (b) shows high Ni count in P2 particles. (d)Raman spectra of samples in cathode form.

Table 2
Raman shifts and the assignment of the Raman spectra of the samples.

Raman shift (cm^{-1})	Assignment	Ref.
340	Mn–O bending	[36]
	Na–O bending	[37]
480	Ni–O/Mn–O 1LO modes	[38]
571	Mn–O symmetrical stretch in MnO_6	[31]
632	Mn–O symmetrical stretch in MnO_6	[31]
1352	D band, from Carbon black	[39]
1593	G band, from Carbon black	[39]

modes are shown in Table 2. Although the band in the 571 cm^{-1} in the pure sample cannot be observed exactly, it can be observed in previous studies, albeit at low intensity [31]. There is a significant increase in the band at 571 cm^{-1} with increasing Ni substitution. The bands at 1352 cm^{-1} and 1593 cm^{-1} indicate the D and G bands, respectively, belonging to carbon black used while preparing electrodes (see Table 2).

The presence of two different phases in NMNO1 and NMNO5 samples causes difficulties in interpreting the results of some general measurements. Therefore, to be more specific, the changes in the valence state and the local environment of the Mn atom with similar symmetry (octahedral) in both the tunnel and P2 phases, Mn–K-edge spectrum measurements were performed.

The comparison of Mn–K edge spectra of NMO, NMNO1 and NMNO5 with Mn_2O_3 (Mn^{+3}) and Li_2MnO_3 (Mn^{+4}) standard samples is shown in Fig. 4(a). The K-edge curves of the samples can be defined as a combination of the standard samples, indicating that both Mn^{+3} and Mn^{+4} exist in the samples. In addition, pre-edge peaks can be seen at 6541 and 6543 eV [40]. The intensity of the peaks belonging to NMNO1, which are seen at approximately 6560 eV (Fig. 4(a)) and called "white line", are lower than the others, while the peaks belonging to NMNO5 and NMO have approximately the same intensity. This result indicates that the NMNO1 sample contains more Mn^{+3} than the other samples.

In Fig. 4(a), it can be seen in detail in the inset, an increase in the Mn^{+4}/Mn^{+3} ratio causes the peaks to shift to high energy. Another important change is seen in the white line: the increase in intensity observed with increasing substitution rate is due to distortions in the MnO_6 octahedral structure [41]. In addition, information about the

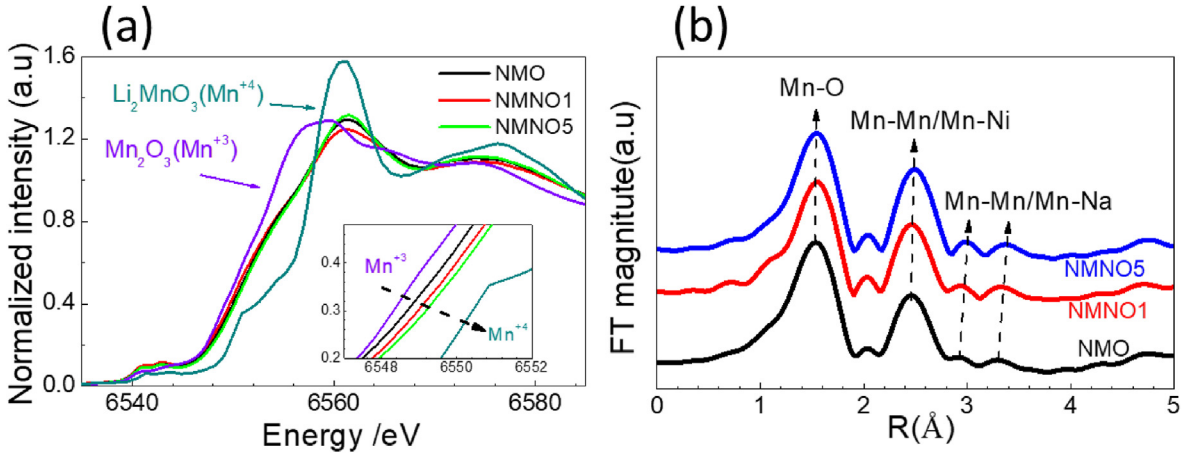

Fig. 4. (a) Mn K-edge spectra of NMO, NMNO1, NMNO5 and standard Mn_2O_3 and Li_2MnO_3 samples. (b) The R-space k^3 – weighted Fourier transform of Mn K-edge EXAFS spectra.

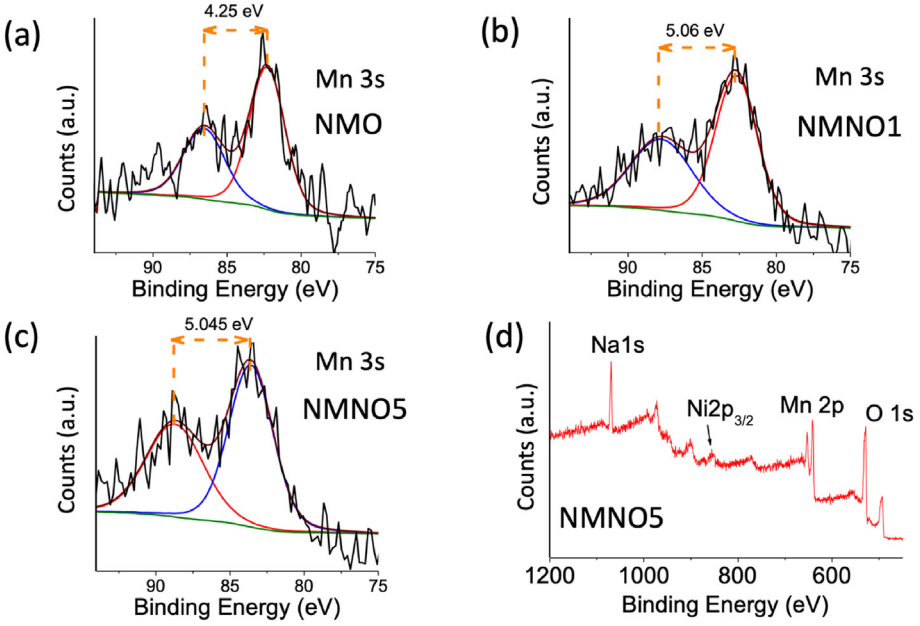

Fig. 5. Mn 3s XP spectra of (a) NMO, (b) NMNO1 and (c) NMNO5. Peaks splitting energy decreases with increasing Ni doping. The survey spectrum of NMNO5 sample (d). In order to clearly see the Ni 2p signal, the survey spectrum of the NMNO5 sample is used.

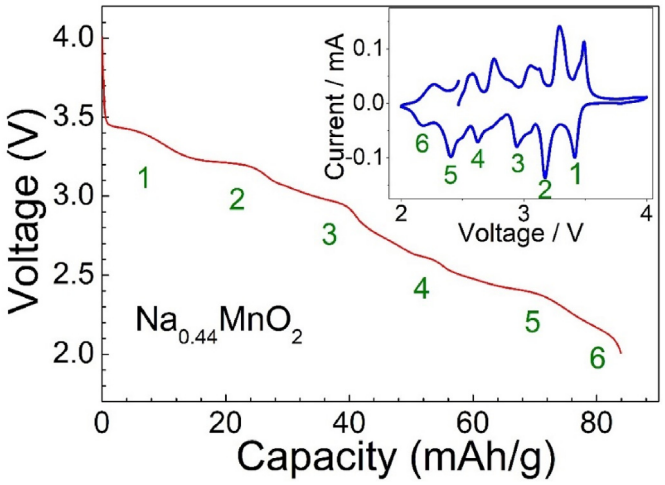

Fig. 6. The initial discharge and CV curve (inset) of bare NMO sample. Equivalent reactions in the both graphs are indicated by the same number.

radial distances of Mn atoms can be obtained by performing FT from Mn K-edge EXAFS data (Fig. 4(b)). Each peak in the spectrum defines the distances of Mn atoms from their nearest neighbors. However, the peaks at 1.9 Å, 2.8 Å and 3.1–3.5 Å belong to Mn–O, Mn-M (M = Mn or Ni) and Mn–Mn/Na coordination shells, respectively [35]. With the increase of Ni substitution, the Mn–O radial distance decreased while the Mn-metal radial distance increased. It can be attributed to the distortion caused by the Ni substitution effect in the MnO_6 octahedral structure. In addition, as the Mn^{+4}/Mn^{+3} ratio increases, the Mn–O radial distance also decreases, because the Mn^{+4}–O bond length is shorter than Mn^{+3}–O [42].

For the quantitative analysis of Mn valence states, the Mn 3s XPS spectrum was performed (Fig. 5). Because of the overlap in binding energy, the complex multiplet splitting, the satellite-loss features and asymmetry of the spectra of the Mn 2p peaks [43–45], the analysis of the Mn 3s doublet splitting is more precise to define the Mn oxidation state [46]. However, it is very difficult to collect Ni signals at the analysis level because the Ni substitution rate is very low. On the other hand, Ni 2p peaks can be observed in the survey spectrum of the NMNO5 sample (Fig. 5(d)), albeit with difficulty. Survey spectrums of all samples can be seen in Fig. S6. The electron exchange between Mn 3s-3d orbitals during the photoemission is the factor that directly affects the energy difference between the splitting Mn 3s peaks [47]. It has been reported that there is an inverse correlation between the Mn 3s peak split energy and the Mn valence state [48]. The splitting energies of NMO, NMNO1 and NMNO5 are 4.82, 4.58, 4.41 eV, respectively. Kim et al. reported that the average valence electron number of Mn can be calculated using the following equation, 7.875-0.893 Δs, where Δs is energy splitting of Mn 3s peaks [49]. According to this equation, the average Mn valence state for NMO, NMNO1 and NMNO5 samples were calculated as 4.08, 3.34 and 3.37, respectively.

In theory, Mn oxidation level distribution is 44% Mn^{+3}, 56% Mn^{+4} and 70% Mn^{+3} and 30% Mn^{+4} in NMO and P2 samples, respectively. Considering the tunnel and P2 phase ratios of NMNO1 and NMNO5 samples, it is expected that the average Mn oxidation is closer to Mn^{+3}. However, the fact that these two samples have approximately the same amount of tunnel and P2 phase may help to better understand the effect of Ni substitution at Mn sites on electrochemical properties.

The matching of the reaction plateaus in the initial discharge and CV curve can be seen in Fig. 6. Both curves reveal that the bare sample NMO has multiple phase transitions. The points identified by 1, 2, 3, and 5 on the curves represent oxidation/reduction reactions at Na2 sites, while 4 and 6 represent reactions at Na3 sites (see Fig. 1(a)) [50].

Fig. 7(a–c) shows the discharge curves of the initial and 100th cycles of NMO, NMNO1 and NMNO5 samples, respectively, at 0.3C (1C = 121

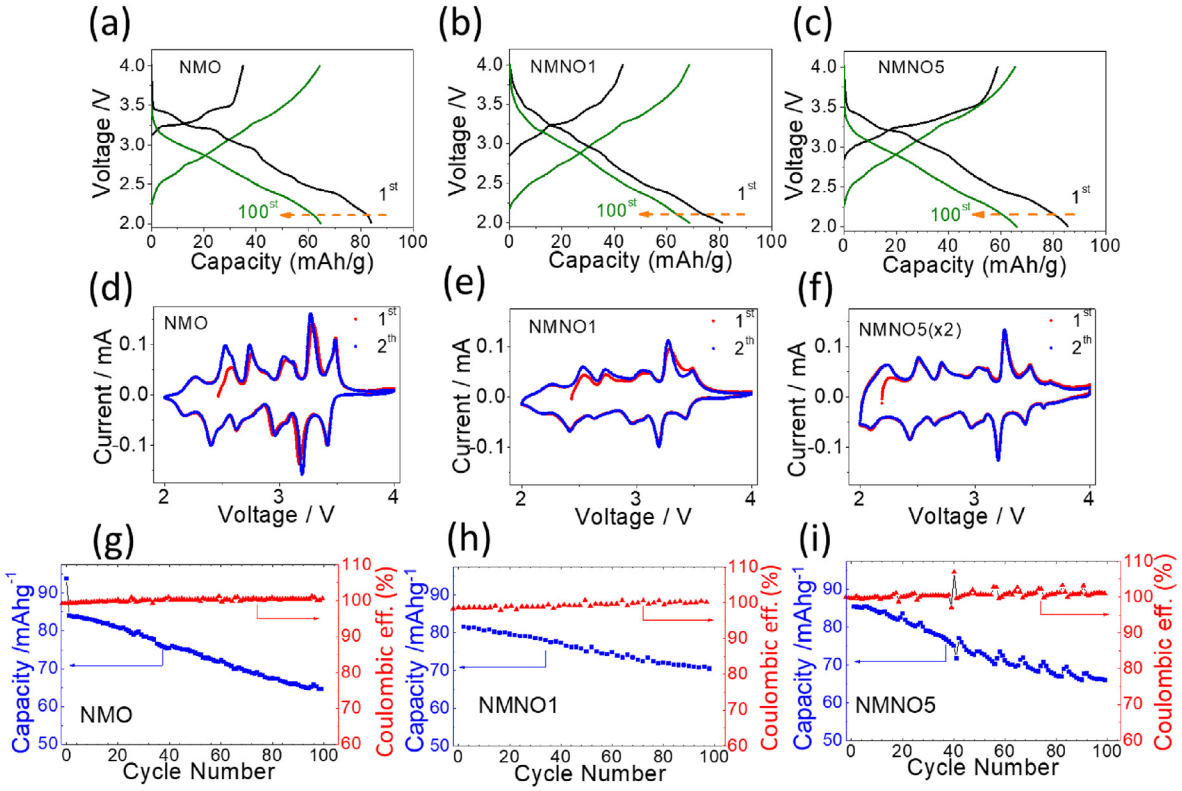

Fig. 7. 1st and 100th discharge/charge curves of (a) NMO, (b) NMNO1 and (c) NMNO5 between 2.0 and 4.0 V potential window at 0.3C current rate vs Na/Na^+. Cyclic voltammetry of (d) NMO, (e) NMNO1 and (f) NMNO5 between a 2.0–4.0 V potential window at a 0.1 mV/s scan rate, and cyclic performance and Coulombic efficiency of (g) NMO, (h) NMNO1, and (j) NMNO5 for 100 cycles.

mAh). The discharge curves of NMNO1 and NMNO5 samples are smoother compared to the pure NMO sample. With this result, it can be

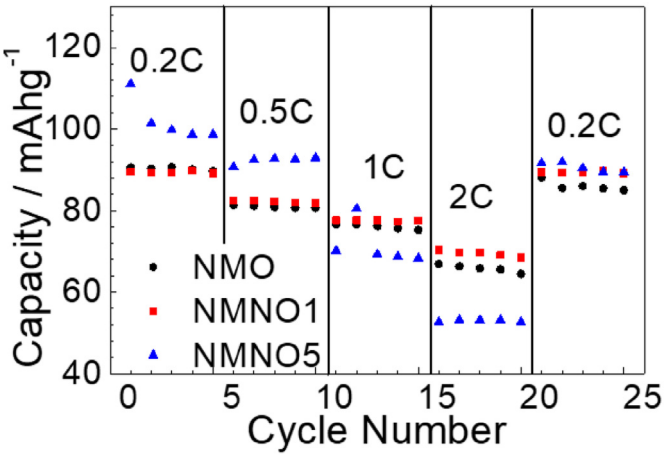

Fig. 8. The rate capability of NMO, NMNO1 and NMNO5 (1C = 121 mAh).

Table 3
Comparison of initial discharge capacities of tunnel (T) and P2 type samples in the literature with NMNO1 and NMNO5 samples.

Sample	Specific Capacity (mAh/g)	Refs.
T-$Na_{0.54}Mn_{0.50}Ti_{0.51}O_2$	83	[53]
T-$Na_{0.44}Mn_{0.89}Ti_{0.11}O_2$	110	[14]
P2-$Na_xMg_{0.11}Mn_{0.89}O_2$	63	[54]
NMNO1	82	In this work
NMNO5	85.5	

concluded that less redox reactions occur at the Na2 and Na3 sites in the crystal structure of NMNO1 and NMNO5 samples compared to the NMO sample in the same voltage range. However, another reason may be that the P2 phase increases with the increase of Ni substitution in the samples; P2 $Na_{0.7}MnO_{2.05}$ discharge curve has a smoother structure. The change in CV curves support this reason.

The CV curves of NMO, NMNO1, and NMNO5 can be seen in Fig. 7 (d)–(f). It can be seen that the cathodic/anodic peaks of NMNO1 and NMNO5 sample in the 2.0–3.0 V range have wider peaks, and this behavior indicate that the Na insertion/extraction reaction time increased. While fast ion diffusion is a well-known feature of the tunnel structure of NMO, this increase in insertion/extraction reaction time was due to the increase in the P2 phase with increasing Ni substitution in the NMNO1 and NMNO5. However, the diminished peak intensity in NMNO1 and NMNO5 samples indicates that phase transitions are successfully suppressed in these samples [51]. Moreover, the smoother discharge curves in these samples are also an indication of phase suppression. Comparison of the cathodic peak positions of the samples can be seen in Table S4.

Fig. 7 (g)–(i) shows the cyclic performance and the Coulombic efficiency (CE) of NMO, NMNO1 and NMNO5, respectively, for 100 cycles at 0.3C. CE is used to describe the Na^+ loss at each cycle. The CEs of the samples are approximately 100%, indicating that the Na insertion/extraction reactions in the cycles are reversible. However, it can be said that the tests are carried out in a half-cell and Na metal is used as the anode which acts as a Na reservoir. Thus, CE will not be accurate for estimating the cycle life of these cells, it will be more meaningful in full-cell tests. However, CE and capacity retention are not directly related. We can also deduce this result from the fact that the samples have approximately the same Coulombic efficiency but different capacity retention rates. The capacity retention of NMO, NMNO1, and NMNO5 was calculated as 77%, 86.4%, and 77.3% after 100 cycles, respectively.

Fig. 8 shows the rate performance of samples in a 2.0–4.0 V potential window at different current rates. All the samples maintain discharge capacity even after 2C rate. The NMO sample has a tunnel-type crystal structure and therefore has high-rate performance because it has wide diffusion paths. However, changes in NMO particle sizes affect the Na diffusion and rate performance. Zahn *et al.* reported that the increase in the diameter of the rods causes a decrease in the capacity and rate performance as it lengthens the Na ion diffusion path [52]. According to the SEM and TEM results, it was revealed that the tunnel-type structures in the NMNO1 and NMNO5 samples thickened with the increase of Ni substitution. Therefore, capacity reduction can be observed in these samples. On the other hand, NMNO1 and NMNO5 samples have P2 phase which can be contribute to rate performance as well as the capacity. Moreover, there is Ni substitution that will reduce the structural deformations of JT active Mn^{+3} in the P2 phase at long cycle tests. However, the reason for the rapid decrease in the rate performance of the NMNO5 sample may be that the tunnel phase is found to be the dominant phase compared to the P2 phase, despite the increased Ni substitution.

Table 3 shows the comparison of initial capacities of the NMNO1 and NMNO5 samples with other TM substituted samples in the literature. The results obtained from NMNO1 and NMNO5 compared to similar TM substitution rates are quite promising for SIBs.

4. Conclusion

The high capacity of NMO and P2 –$Na_{0.7}MnO_{2.05}$ makes them highly attractive candidates for more efficient SIBs. However, phase transitions and JT effect on Mn^{+3} during charge/discharge cycles causes structural degradations and capacity loss. Here, we purpose to improve the cycling performance and one step synthesis of a composite material by Ni cation doping into NMO.

XRD results show that the NMO material was successfully synthesized and the P2 phase started to form in NMNO1 and NMNO5 materials with Ni substitution. The decrease in volume observed in the NMO phase can be explained by the separation of Na from the NMO structure for the formation of the P2 phase.

XAS analysis results reveal that Ni substitution reduces the number of Mn^{+3} in the samples, which is supported by magnetism measurement. The decrease in the number of Mn^{+3} in octahedral structures affected by JT also causes a decrease in crystal structure degradation at long cycle numbers.

The surface morphology images of the samples show that Ni substitution causes the P2 phase to form next to the rod-like structure. Both phases are clearly observed in these images. EDS and mapping results show that Ni tends to substitute for the P2 structure.

The voltage-capacity results of the samples show that bi-phasic samples have smoother curves. Therefore, it can be concluded that these samples have less phase transitions during their charge/discharge cycles. The change in CV graphics also supports this result. The decrease in the phase transition means that the deformation of the crystal structures also decreases, which is reflected in the 100 cycle performances of the samples and bi-phasic samples show higher cyclic efficiency than the NMO sample. Moreover, structural stabilization was able to give the capacity in the first cycle at 0.2C after 2C high current charge/discharge.

The Ni doping maintained the cycling stability and Coulombic efficiency of the material. This structural modification suppressed phase transition and JT effect during charge/discharge, resulting in superior cycling performance compared to pristine T-$Na_{0.44}MnO_2$.

CRediT authorship contribution statement

Erdinc Oz: Conceptualization, Methodology, Data curation, Writing – original draft. **Serdar Altin:** Investigation, Supervision, Writing – review & editing. **Sevda Avci:** Investigation, Supervision, Writing – review & editing.

Declaration of competing interest

The authors declare that they have no known competing financial interests or personal relationships that could have appeared to influence the work reported in this paper.

Data availability

Data will be made available on request.

Acknowledgements

E. Oz and S. Altin would like to thank for financial support of the Inonu University Scientific Research Project Unit (IUBAP) (project no: FDK-2017/678). E. Oz would like to thank Ankara University Institute of Accelerator Technologies (TARLA) (project no:2006K-12047) and Deutsches Elektronen-Synchrotron (DESY) research institute. The research also partly supported by Horizon 2020 pilot NFFA.EU project (project ID-568). We gratefully acknowledge the funding of the potentiostat within the PIER Seed Project under contract number PIF-2013-21. S. Avci would like to acknowledge the financial support of the Istanbul Medeniyet University under project number F-GAP-2019-1498. Authors would like to thank to Prof. Sefik Suzer from Bilkent University for XPS measurements and analysis support.

Appendix A. Supplementary data

Supplementary data to this article can be found online at https://doi.org/10.1016/j.jssc.2022.123741.

References

[1] W.G. Mumme, IUCr, the Structure of Na4Mn4Ti5O18, Urn:Issn:0567-7408, vol. 24, 1968, pp. 1114–1120, https://doi.org/10.1107/S0567740868003778.
[2] J.P. Parant, R. Olazcuaga, M. Devalette, C. Fouassier, P. Hagenmuller, Sur quelques nouvelles phases de formule NaxMnO2 (x ≤ 1), J. Solid State Chem. 3 (1971) 1–11, https://doi.org/10.1016/0022-4596(71)90001-6.
[3] Z. Zhao, X. Huang, Y. Shao, S. Xu, L. Chen, L. Shi, Q. Yi, C. Shang, D. Zhang, Surface modification of Na0.44MnO2 via a nonaqueous solution-assisted coating for ultra-Stable and High-Rate sodium-ion batteries, Chemical Engineering Journal Advances 10 (2022), 100292, https://doi.org/10.1016/J.CEJA.2022.100292.
[4] E. Hosono, H. Matsuda, I. Honma, S. Fujihara, M. Ichihara, H. Zhou, Synthesis of single crystalline electro-conductive Na0.44MnO2 nanowires with high aspect ratio for the fast charge–discharge Li ion battery, J. Power Sources 182 (2008) 349–352, https://doi.org/10.1016/J.JPOWSOUR.2008.03.067.
[5] B. Fu, X. Zhou, Y. Wang, High-rate performance electrospun Na0.44MnO2 nanofibers as cathode material for sodium-ion batteries, J. Power Sources 310 (2016) 102–108, https://doi.org/10.1016/J.JPOWSOUR.2016.01.101.
[6] X. He, J. Wang, B. Qiu, E. Paillard, C. Ma, X. Cao, H. Liu, M.C. Stan, H. Liu, T. Gallash, Y.S. Meng, J. Li, Durable high-rate capability Na0.44MnO2 cathode material for sodium-ion batteries, Nano Energy 27 (2016) 602–610, https://doi.org/10.1016/J.NANOEN.2016.07.021.
[7] K.Y. Shen, M. Lengyel, L. Wang, R.L. Axelbaum, Spray pyrolysis and electrochemical performance of Na0.44MnO2 for sodium-ion battery cathodes, MRS Commun 7 (2017) 74–77, https://doi.org/10.1557/MRC.2017.4/FIGURES/4.
[8] M. Xu, Y. Niu, C. Chen, J. Song, S. Bao, C.M. Li, Synthesis and application of ultra-long Na0.44MnO2 submicron slabs as a cathode material for Na-ion batteries, RSC Adv. 4 (2014) 38140–38143, https://doi.org/10.1039/C4RA07355J.
[9] D.J. Kim, R. Ponraj, A.G. Kannan, H.W. Lee, R. Fathi, R. Ruffo, C.M. Mari, D.K. Kim, Diffusion behavior of sodium ions in Na0.44MnO2 in aqueous and non-aqueous electrolytes, J. Power Sources 244 (2013) 758–763, https://doi.org/10.1016/J.JPOWSOUR.2013.02.090.
[10] V. Dall'Asta, D. Buchholz, L.G. Chagas, X. Dou, C. Ferrara, E. Quartarone, C. Tealdi, S. Passerini, Aqueous processing of Na0.44MnO2 cathode material for the development of greener Na-ion batteries, ACS Appl. Mater. Interfaces 9 (2017) 34891–34899, https://doi.org/10.1021/ACSAMI.7B09464/ASSET/IMAGES/LARGE/AM-2017-09464Q_0005.JPEG.
[11] A. Mendiboure, C. Delmas, P. Hagenmuller, Electrochemical intercalation and deintercalation of NaxMnO2 bronzes, J. Solid State Chem. 57 (1985) 323–331, https://doi.org/10.1016/0022-4596(85)90194-X.
[12] D. Kim, M. Cho, K. Cho, D. Kim, M. Cho, K. Cho, Rational Design of Na(Li1/3Mn2/3)O2 operated by anionic redox reactions for advanced sodium-ion batteries, Adv. Mater. 29 (2017), 1701788, https://doi.org/10.1002/ADMA.201701788.
[13] X. Li, X. Ma, D. Su, L. Liu, R. Chisnell, S.P. Ong, H. Chen, A. Toumar, J.C. Idrobo, Y. Lei, J. Bai, F. Wang, J.W. Lynn, Y.S. Lee, G. Ceder, Direct visualization of the Jahn–Teller effect coupled to Na ordering in Na5/8MnO2, Nat. Mater. 13 (2014) 586–592, https://doi.org/10.1038/nmat3964, 6. 13 (2014.
[14] Y. Wang, J. Liu, B. Lee, R. Qiao, Z. Yang, S. Xu, X. Yu, L. Gu, Y.S. Hu, W. Yang, K. Kang, H. Li, X.Q. Yang, L. Chen, X. Huang, Ti-substituted tunnel-type Na0.44MnO2 oxide as a negative electrode for aqueous sodium-ion batteries, Nat. Commun. 6 (2015) 1–10, https://doi.org/10.1038/ncomms7401, 1. 6 (2015).
[15] J. Zhang, D.Y.W. Yu, Stabilizing Na0.7MnO2 cathode for Na-ion battery via a single-step surface coating and doping process, J. Power Sources 391 (2018) 106–112, https://doi.org/10.1016/J.JPOWSOUR.2018.04.077.
[16] C. Luo, A. Langrock, X. Fan, Y. Liang, C. Wang, P2-type transition metal oxides for high performance Na-ion battery cathodes, J Mater Chem A Mater 5 (2017) 18214–18220, https://doi.org/10.1039/C7TA04515H.
[17] E. de La Llave, E. Talaie, E. Levi, P.K. Nayak, M. Dixit, P.T. Rao, P. Hartmann, F. Chesneau, D.T. Major, M. Greenstein, D. Aurbach, L.F. Nazar, Improving energy density and structural stability of manganese oxide cathodes for Na-ion batteries by structural lithium substitution, Chem. Mater. 28 (2016) 9064–9076, https://doi.org/10.1021/ACS.CHEMMATER.6B04078/ASSET/IMAGES/LARGE/CM-2016-04078D_0013.JPEG.
[18] D. Buchholz, C. Vaalma, L.G. Chagas, S. Passerini, Mg-doping for improved long-term cyclability of layered Na-ion cathode materials – the example of P2-type NaxMg0.11Mn0.89O2, J. Power Sources 282 (2015) 581–585, https://doi.org/10.1016/J.JPOWSOUR.2015.02.069.
[19] P. Bai, K. Jiang, X. Zhang, J. Xu, S. Guo, H. Zhou, Ni-doped layered manganese oxide as a stable cathode for potassium-ion batteries, ACS Appl. Mater. Interfaces 12 (2020), https://doi.org/10.1021/ACSAMI.9B22237/ASSET/IMAGES/LARGE/AM9B22237_0003.JPEG.
[20] E.S. Lee, A. Huq, H.Y. Chang, A. Manthiram, High-voltage, high-energy layered-spinel composite cathodes with superior cycle Life for lithium-ion batteries, Chem. Mater. 24 (2012), https://doi.org/10.1021/cm2034992.
[21] Z.G. Wu, J.T. Li, Y.J. Zhong, X.D. Guo, L. Huang, B.H. Zhong, D.A. Agyeman, J.M. Lim, D.H. Kim, M.H. Cho, Y.M. Kang, Mn-based cathode with synergetic layered-tunnel hybrid structures and their enhanced electrochemical performance in sodium ion batteries, ACS Appl. Mater. Interfaces 9 (2017) 21267–21275, https://doi.org/10.1021/ACSAMI.7B04338.
[22] J. Qu, T. Sheng, Z. guo Wu, T. ru Chen, H. Chen, Z. guang Yang, X. dong Guo, J. tao Li, B. he Zhong, X. shi Dou, Unexpected effects of zirconium-doping in the high performance sodium manganese-based layer-tunnel cathode, J Mater Chem A Mater 6 (2018) 13934–13942, https://doi.org/10.1039/C8TA04818E.
[23] J. Rodríguez-Carvajal, Recent advances in magnetic structure determination by neutron powder diffraction, Phys. B Condens. Matter 192 (1993) 55–69, https://doi.org/10.1016/0921-4526(93)90108-I.
[24] P.A. Gokturk, S. Suzer, Probing the dynamics of non-faradaic processes in ionic liquids at extended time and length scales using xps with ac modulation, J. Phys. Chem. C 125 (2021) 9453–9460, https://doi.org/10.1021/ACS.JPCC.1C01292/ASSET/IMAGES/LARGE/JP1C01292_0006.JPEG.
[25] H. Kim, D.J. Kim, D.H. Seo, M.S. Yeom, K. Kang, D.K. Kim, Y. Jung, Ab initio study of the sodium intercalation and intermediate phases in Na 0.44MnO 2 for sodium-ion battery, Chem. Mater. 24 (2012) 1205–1211, https://doi.org/10.1021/CM300065Y/SUPPL_FILE/CM300065Y_SI_001.PDF.
[26] M.M. Doeff, T.J. Richardson, K.T. Hwang, Electrochemical and structural characterization of titanium-substituted manganese oxides based on Na0.44MnO2, J. Power Sources 135 (2004) 240–248, https://doi.org/10.1016/J.JPOWSOUR.2004.03.073.
[27] M.M. Doeff, T.J. Richardson, L. Kepley, Lithium insertion processes of orthorhombic Na x MnO2-based electrode materials, J. Electrochem. Soc. 143 (1996) 2507–2516, https://doi.org/10.1149/1.1837039/XML.
[28] X. Zhou, R.K. Guduru, P. Mohanty, Synthesis and characterization of Na0.44MnO2 from solution precursors, J Mater Chem A Mater 1 (2013) 2757–2761, https://doi.org/10.1039/C3TA01134H.
[29] T. Sun, X. Yao, Y. Luo, M. Fang, M. Shui, J. Shu, Y. Ren, Micron-sized Na0.7MnO2.05 as cathode materials for aqueous rechargeable magnesium-ion batteries, Ionics 25 (2019) 4805–4815, https://doi.org/10.1007/S11581-019-03057-7/FIGURES/8.
[30] D. Su, C. Wang, H.J. Ahn, G. Wang, Single crystalline Na0.7MnO2 nanoplates as cathode materials for sodium-ion batteries with enhanced performance, Chem. Eur J. 19 (2013) 10884–10889, https://doi.org/10.1002/CHEM.201301563.
[31] L. Zhao, J. Ni, H. Wang, L. Gao, Na0.44MnO2–CNT electrodes for non-aqueous sodium batteries, RSC Adv. 3 (2013) 6650–6655, https://doi.org/10.1039/C3RA23032E.
[32] M.S. Chae, H.J. Kim, H. Bu, J. Lyoo, R. Attias, B. Dlugatch, M. Oliel, Y. Gofer, S.-T. Hong, D. Aurbach, M.S. Chae, R. Attias, B. Dlugatch, M. Oliel, Y. Gofer, D. Aurbach, H.J. Kim, H. Bu, J. Lyoo, S. Hong, The sodium storage mechanism in tunnel-type Na0.44MnO2 cathodes and the way to ensure their durable operation, Adv. Energy Mater. 10 (2020), 2000564, https://doi.org/10.1002/AENM.202000564.
[33] J. Qu, D. Wang, Z.G. Yang, Z.G. Wu, L. Qiu, X.D. Guo, J.T. Li, B.H. Zhong, X.C. Chen, S.X. Dou, Ion-doping-site-variation-induced composite cathode adjustment: a case study of layer-tunnel Na0.6MnO2 with Mg2+ doping at Na/Mn site, ACS Appl. Mater. Interfaces 11 (2019) 26938–26945, https://doi.org/10.1021/ACSAMI.9B07865/ASSET/IMAGES/LARGE/AM-2019-07865B_0008.JPEG.
[34] T.E. Fan, S.M. Liu, X. Tang, Z.H. Zou, J.Q. Xie, M.Y. Wang, Rational construction of Na0.44MnO2 nanorods and PAN nanofibers composite as high areal capacity sodium-ion batteries, Ionics 27 (2021) 1137–1142, https://doi.org/10.1007/S11581-021-03910-8/TABLES/1.
[35] R.D. Shannon, IUCr, Revised Effective Ionic Radii and Systematic Studies of Interatomic Distances in Halides and Chalcogenides, Urn:Issn:0567-7394, vol. 32, 1976, pp. 751–767, https://doi.org/10.1107/S0567739476001551.

[36] Y. Lin, S. Zhao, J. Qian, N. Xu, X.Q. Liu, L.B. Sun, W. Li, Z. Chen, Z. Wu, Petal cell-derived MnO nanoparticle-incorporated biocarbon composite and its enhanced lithium storage performance, J. Mater. Sci. 55 (2020) 2139–2154, https://doi.org/10.1007/S10853-019-04085-4/FIGURES/12.

[37] M. Sendova-Vassileva, R. Stoyanova, D. Carlier, M. Yoncheva, E. Zhecheva, C. Delmas, Raman spectroscopy study on Na2/3Mn1-xFexO2 oxides, Adv. Sci. Technol. 74 (2010) 60–65, https://doi.org/10.4028/WWW.SCIENTIFIC.NET/AST.74.60.

[38] O. Lupan, S. Koussi-Daoud, B. Viana, T. Pauporté, Oxide planar p–n heterojunction prepared by low temperature solution growth for UV-photodetector applications, RSC Adv. 6 (2016) 68254–68260, https://doi.org/10.1039/C6RA13763F.

[39] R. Rao, R. Podila, R. Tsuchikawa, J. Katoch, D. Tishler, A.M. Rao, M. Ishigami, Effects of layer stacking on the combination Raman modes in graphene, ACS Nano 5 (2011) 1594–1599, https://doi.org/10.1021/NN1031017/SUPPL_FILE/NN1031017_SI_001.PDF.

[40] J.E. Hahn, R.A. Scott, K.O. Hodgson, S. Doniach, S.R. Desjardins, E.I. Solomon, Observation of an electric quadrupole transition in the X-ray absorption spectrum of a Cu(II) complex, Chem. Phys. Lett. 88 (1982) 595–598, https://doi.org/10.1016/0009-2614(82)85016-1.

[41] V. Cuartero, S. Lafuerza, M. Rovezzi, J. García, J. Blasco, G. Subías, E. Jiménez, X-ray absorption and emission spectroscopy study of Mn and Co valence and spin states in TbM n 1-x C ox O 3, Phys. Rev. B 94 (2016), 155117, https://doi.org/10.1103/PHYSREVB.94.155117/FIGURES/13/MEDIUM.

[42] J. Akimoto, H. Hayakawa, N. Kijima, J. Awaka, F. Funabiki, Single-crystal synthesis and structure refinement of Na0.44MnO2, Solid State Phenom. 170 (2011) 198–202, https://doi.org/10.4028/WWW.SCIENTIFIC.NET/SSP.170.198.

[43] G. Yan, Y. Lian, Y. Gu, C. Yang, H. Sun, Q. Mu, Q. Li, W. Zhu, X. Zheng, M. Chen, J. Zhu, Z. Deng, Y. Peng, Phase and morphology transformation of MnO2 induced by ionic liquids toward efficient water oxidation, ACS Catal. 8 (2018) 10137–10147, https://doi.org/10.1021/ACSCATAL.8B02203/ASSET/IMAGES/MEDIUM/CS-2018-022035_0007.GIF.

[44] M. Chigane, M. Ishikawa, Manganese oxide thin film preparation by potentiostatic electrolyses and electrochromism, J. Electrochem. Soc. 147 (2000) 2246, https://doi.org/10.1149/1.1393515/XML.

[45] M. Chigane, M. Ishikawa, M. Izaki, Preparation of manganese oxide thin films by electrolysis/chemical deposition and electrochromism, J. Electrochem. Soc. 148 (2001) D96, https://doi.org/10.1149/1.1376637/XML.

[46] E. Hastuti, A. Subhan, P. Amonpattaratkit, M. Zainuri, S. Suasmoro, The effects of Fe-doping on MnO2: phase transitions, defect structures and its influence on electrical properties, RSC Adv. 11 (2021) 7808–7823, https://doi.org/10.1039/D0RA10376D.

[47] E.M. Erickson, H. Sclar, F. Schipper, J. Liu, R. Tian, C. Ghanty, L. Burstein, N. Leifer, J. Grinblat, M. Talianker, J.Y. Shin, J.K. Lampert, B. Markovsky, A.I. Frenkel, D. Aurbach, High-temperature treatment of Li-rich cathode materials with ammonia: improved capacity and mean voltage stability during cycling, Adv. Energy Mater. 7 (2017), 1700708, https://doi.org/10.1002/AENM.201700708.

[48] M. Fujiwara, T. Matsushita, S. Ikeda, Evaluation of Mn3s X-ray photoelectron spectroscopy for characterization of manganese complexes, J. Electron. Spectrosc. Relat. Phenom. 74 (1995) 201–206, https://doi.org/10.1016/0368-2048(94)02375-1.

[49] J. Song, J. Gim, S. Kim, J. Kang, V. Mathew, D. Ahn, J. Kim, A sodium manganese oxide cathode by facile reduction for sodium batteries, Chem. Asian J. 9 (2014) 1550–1556, https://doi.org/10.1002/ASIA.201301510.

[50] H. Kim, D.J. Kim, D.H. Seo, M.S. Yeom, K. Kang, D.K. Kim, Y. Jung, Ab initio study of the sodium intercalation and intermediate phases in Na 0.44MnO 2 for sodium-ion battery, Chem. Mater. 24 (2012) 1205–1211, https://doi.org/10.1021/CM300065Y/SUPPL_FILE/CM300065Y_SI_001.PDF.

[51] H. Li, M. Cormier, N. Zhang, J. Inglis, J. Li, J.R. Dahn, Is cobalt needed in Ni-rich positive electrode materials for lithium ion batteries? J. Electrochem. Soc. 166 (2019) A429, https://doi.org/10.1149/2.1381902JES.

[52] P. Zhan, K. Jiao, J. Wang, Z. Hu, R. Ma, H. Zhu, S. Jiao, Titanium-substituted Na 0.44 MnO 2 nanorods as cathode materials for high performance sodium-ion batteries, J. Electrochem. Soc. 162 (2015) A2296–A2301, https://doi.org/10.1149/2.0521512JES/XML.

[53] X. Jiang, S. Liu, H. Xu, L. Chen, J. Yang, Y. Qian, Tunnel-structured Na0.54Mn0.50Ti0.51O2 and Na0.54Mn0.50Ti0.51O2/C nanorods as advanced cathode materials for sodium-ion batteries, Chem. Commun. 51 (2015) 8480–8483, https://doi.org/10.1039/C5CC02233A.

[54] D. Buchholz, C. Vaalma, L.G. Chagas, S. Passerini, Mg-doping for improved long-term cyclability of layered Na-ion cathode materials – the example of P2-type NaxMg0.11Mn0.89O2, J. Power Sources 282 (2015) 581–585, https://doi.org/10.1016/J.JPOWSOUR.2015.02.069.